Supporting Information

3D Dendritic Hierarchically Gradient Nanoflowers *In Situ* Grown on Conductive Substrates for Efficient Hydrovoltaic Power Generation

Yanan Wang,[a,b] Xianrong Yuan,[a,b] Kun Ni,[b,c] Yuhang Song,[a,b] Xiang Li,[a,b] Xuelian Zeng,[a,b] Beibei Shao*[a,b] and Baoquan Sun*[a,b,d]

[a]Jiangsu Key Laboratory for Carbon-Based Functional Materials & Devices, Institute of Functional Nano & Soft Materials (FUNSOM), Soochow University, Suzhou 215123, PR China.
[b]Jiangsu Key Laboratory of Advanced Negative Carbon Technologies, Soochow University, Suzhou 215123, P. R. China.
[c]Key Laboratory for Advanced Carbon Materials and Wearable Energy Technologies of Jiangsu Province, College of Energy, Soochow University, Suzhou 215006, P. R. China.
[d]Macau Institute of Materials Science and Engineering MUST-SUDA Joint Research Center for Advanced Functional Materials Macau University of Science and Technology Macau 999078, P. R. China.

E-mail: bbshao@suda.edu.cn, bqsun@suda.edu.cn

This PDF file includes:

Supporting Information 1. Numerical simulation of the concentration distribution of hydrogen ions and hydroxides based on 2D nanochannels

The concentration distribution of ions and surface charge density distribution were both numerically calculated by using the commercial finite-element software package COMSOL (version 5.6) Multiphysics based on the built-in coupled two-dimensional Nernst-Planck-Poisson (PNP) equations. The model is simplified by assuming steady-state conditions, and considering the modeling and computational complexity of three-dimensional models, a 2D model is adopted to explore the concentration distribution of hydrogen ions and hydroxides in nanochannels with different diameters. The active layer is composed of TiO_2 nanoflowers, and the macroporous channels between nanoflowers and mesoporous channels between the blocks that form nanoflowers constitute a rich pore structure. The size of nanoflowers is extremely close and the reaction conditions are the same at different concentrations, the simulation analysis focused on the most obvious difference between the different kinds of nanoflowers, the mesoporous channel of different sizes.

The numerical simulation model based on 2D structure is shown in Fig. 5c. It contains a negatively charged active layer representing the channels between the nanorods blocks that comprise the TiO_2 nanoflowers. Only the pore size varies, and the surface charge density, initial ion concentration, and boundary conditions remain unchanged. And the surface charge was set as negative here.

The PNP equations are recalled below [1,2]:

The Nernst-Planck equation describes the fluxes of mobile ions and transport properties of a charged nanochannel:

$$j_i = D_i\left(\nabla c_i + \frac{z_i F c_i}{RT}\nabla\varphi\right) \quad (1)$$

The Poisson equation defines the relationship between the electrical potential and ion concentrations:

$$\nabla^2\varphi = -\frac{F}{\varepsilon}\sum z_i c_i \quad (2)$$

When the system reaches a stationary regime, the flux must satisfy the following equation:

$$\nabla \cdot j_i = 0 \quad (3)$$

Above j_i, D_i, c_i, z_i, φ, ε, F, R, and T are the ionic flux, diffusion coefficient, ion concentration, valence number for each species i, electrical potential, dielectric constant of the solution, faraday constant, universal gas constant, and absolute temperature, respectively.

The ion flux has the zero normal components at boundaries:

$$n \cdot j_i = 0 \quad (4)$$

The boundary condition for the potential φ on the channel walls is:

$$n \cdot \nabla\varphi = -\frac{\sigma}{\varepsilon} \quad (5)$$

where σ represents the surface charge density. The formation of the electric field is considered to be due to the different surface charge densities of the heterostructure. Therefore, the surface charge density of the TiO_2 nanoflowers is set to be $-2e^{-5}$ C m^{-2}. The initial concentration of the mobile ions (H^+ and OH^-) in the left reservoir is set to 10^{-10} mol L^{-1} and the right reservoirs are set to 10^{-7} mol L^{-1}. The surface charge density of the water reservoir is set to 0 C m^{-2}. With the given geometry and suitable boundary conditions, the coupled PNP equations are solved with finite-element calculations for the ion concentration distribution.

Supporting Information 2. Representative electricity output performance of the hydrovoltaic devices

Table S1. Electricity performance of some recently reported hydrovoltaic devices based on low-dimensional nanomaterials with inert electrodes.

Reference	Functional materials	Short-circuit current density ($\mu A \cdot cm^{-2}$)	Electrodes
Ref. 1[3]	TiO_2 nanoparticles	0.12	CNT paste
Ref. 2[4]	CuO nanowires	2.49	---
Ref. 3[5]	TiO_2 nanowires	8	ITO
Ref. 4[6]	Al_2O_3 nanoparticles	0.80	Carbon paste
Ref. 5[7]	PVDF-SiO_2-TiO_2-Glass fiber	1.45	CNT paste
Ref. 6[8]	TiO_2/CNT	0.25	Carbon paste
Ref. 7[9]	SiNWs	13	CNT mesh paper
Ref. 8[10]	SiNWs	22	Graphite/PEDOT: PSS/fabric
This work	TiO_2 nanoflowers	45	CNT mesh paper

Supporting Information 3. Porosity properties of as-prepared 3D hierarchical TiO_2 nanoflowers

Table S2. Porosity properties of as-prepared 3D HTNFs with different precursor concentrations.

Samples	S_{bet} ($m^2 \cdot g^{-1}$)	V_{micro} ($cm^3 \cdot g^{-1}$)	V_{meso} ($cm^3 \cdot g^{-1}$)	V_{total} ($cm^3 \cdot g^{-1}$)
HTNFs-3	4.10	0.042	0.054	0.096
HTNFs-6	6.09	0.12	0.047	0.167
HTNFs-9	7.45	0.20	0.04	0.24

Supporting Information 4. Analysis of variance (ANOVA) results of different influential factors

Table S3. The specific value of the ANOVA results from different factors.

	Mean	**Mean SEM**	**F value**	**Prob>F**
Plasma treatment time	427.87	33.09	---	---
Thickness	514.5	20.91	---	---
Water volume	449.1	50.44	---	---
Water temperature	524.23	27.61	---	---
Ion concentration	529.6	13.01	---	---
Polarity solution type	504.07	23.14	---	---
Factor	---	---	**1.92**	**0.099**

*SEM: standard error of the mean

Supporting Information 5. Characterization of the top electrode

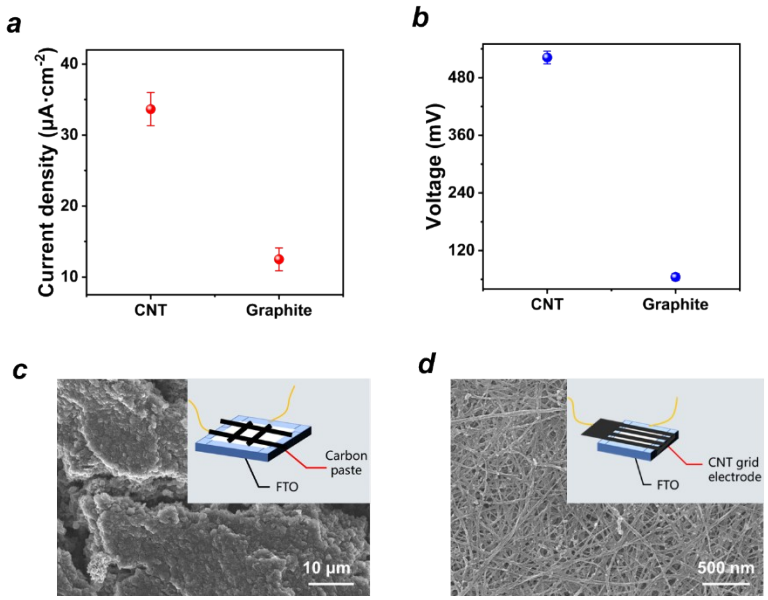

Fig. S1. Electricity output and morphology comparison of 3D hierarchical TiO_2 nano-flowers based WDHPGs with different top electrodes. (a) Short-circuit current density and (b) open-circuit voltage values of corresponding devices. Schematic and scanning electron microscope (SEM) images of (c) grid carbon paste and (d) carbon nanotube (CNT) mesh paper.

Supporting Information 6. Synthesis process of 3D hierarchical TiO_2 nanoflowers (3D HTNFs)

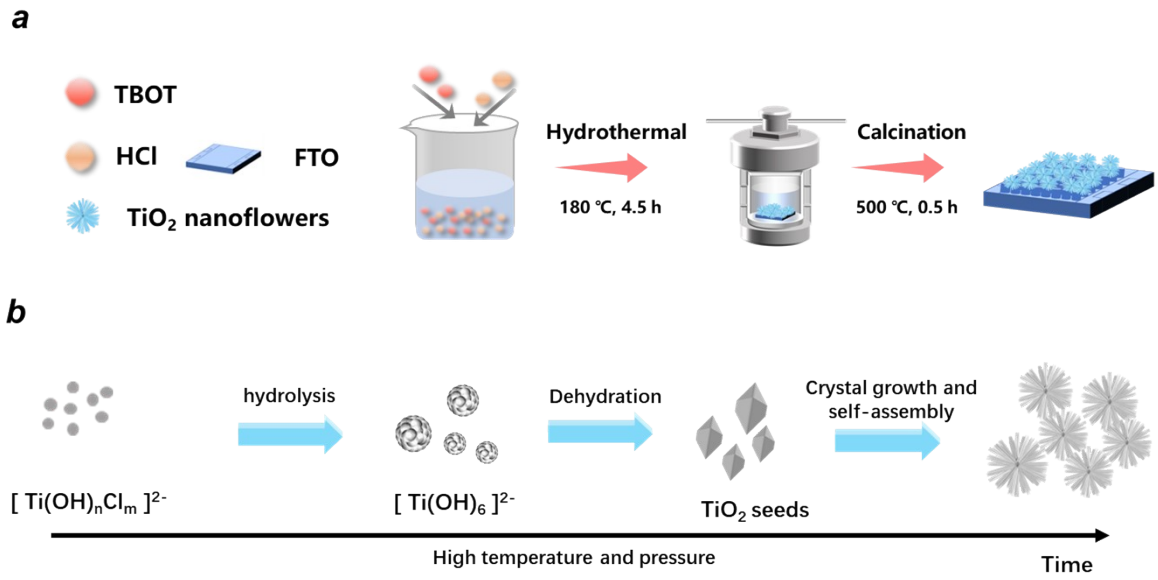

Fig. S2. Schematic illustration of the (a) synthesis process of 3D hierarchical TiO_2 nano-flowers that include hydrothermal synthesis and calcination and the (b) detailed formation process of 3D HTNFs, respectively.

Supporting Information 7. Chemical bonds and functional groups of obtained 3D HTNFs

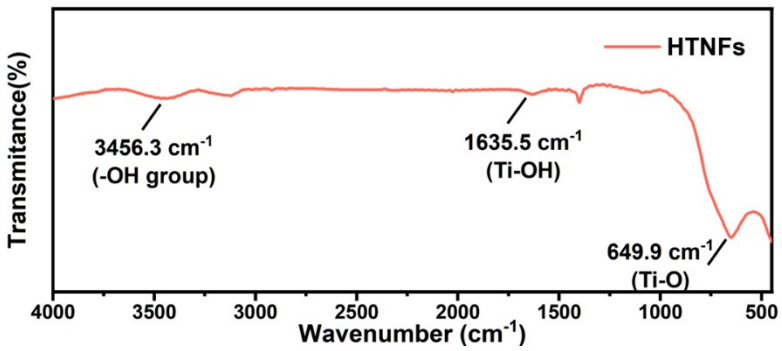

Fig. S3. Fourier transform infrared spectroscopy (FTIR) spectrum of 3D hierarchical TiO_2 nanoflowers.

Supporting Information 8. Surface charge density measurement of obtained 3D HTNFs

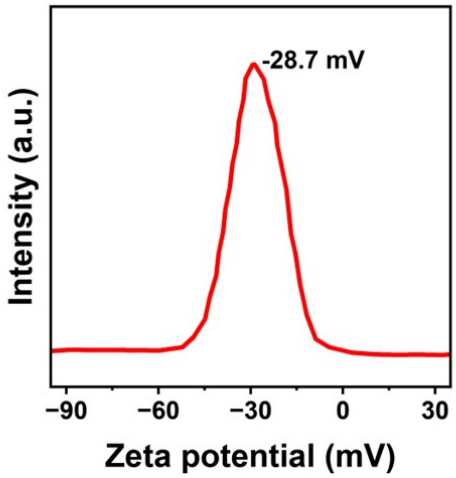

Fig. S4. Zeta potential measurement of 3D hierarchical TiO_2 nanoflowers.

Supporting Information 9. Surface charge density changes under different plasma treatment time

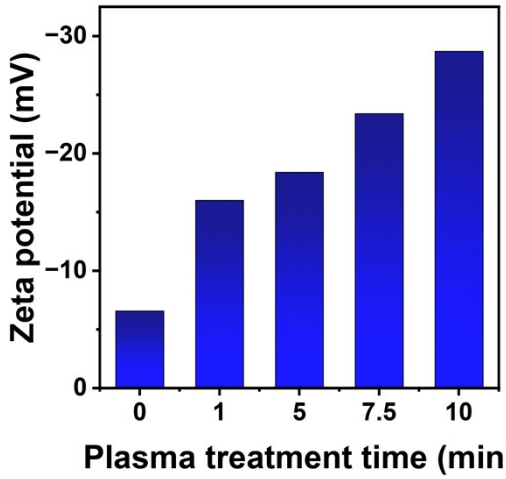

Fig. S5. The influence of the plasma treatment time on the Zeta potential of 3D hierarchical TiO_2 nanoflowers.

Supporting Information 10. Thickness changes with different holding time

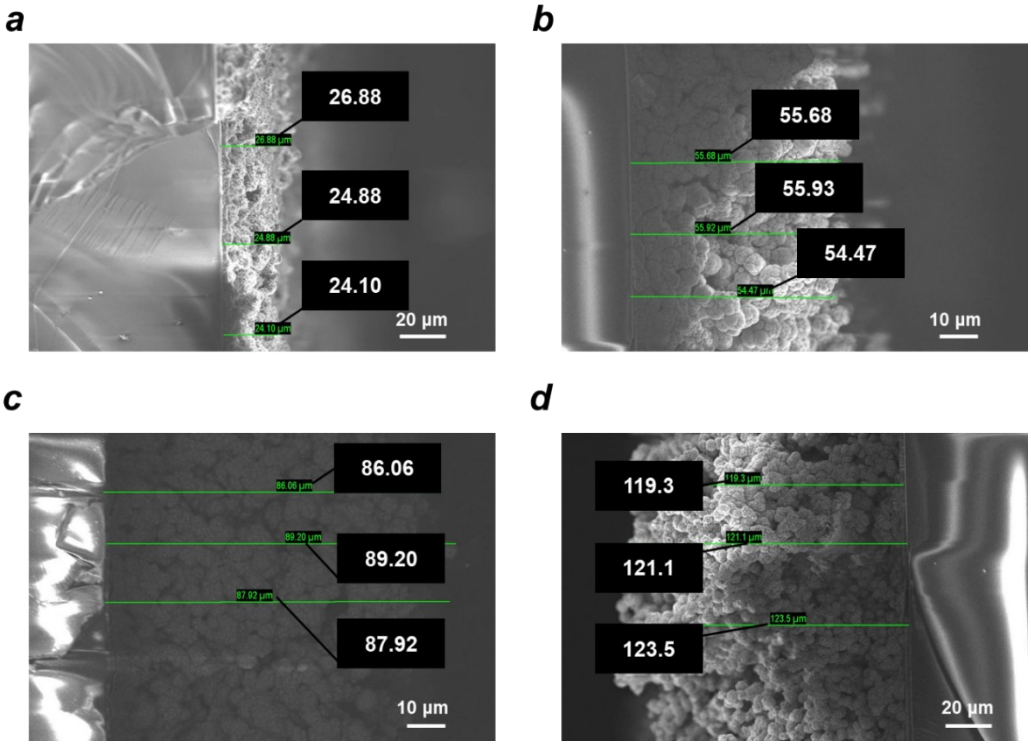

Fig. S6. The side-view SEM images of the 3D HTNFs layer with different holding times (a) 1.5 h, (b) 3 h, (c) 4.5 h, and (d) 6 h in the hydrothermal synthesis.

Supporting Information 11. Electrical performance under different water droplets

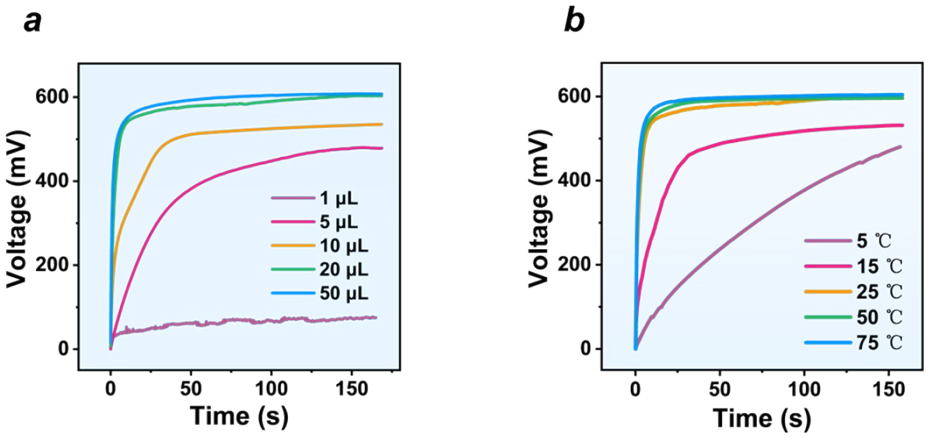

Fig. S7. Voltage-time curve of WDHPGs based on 3D hierarchical TiO_2 nanoflowers under dripping water of different (a) volumes and (b) temperatures.

Supporting Information 12. Response to subsequent water droplet

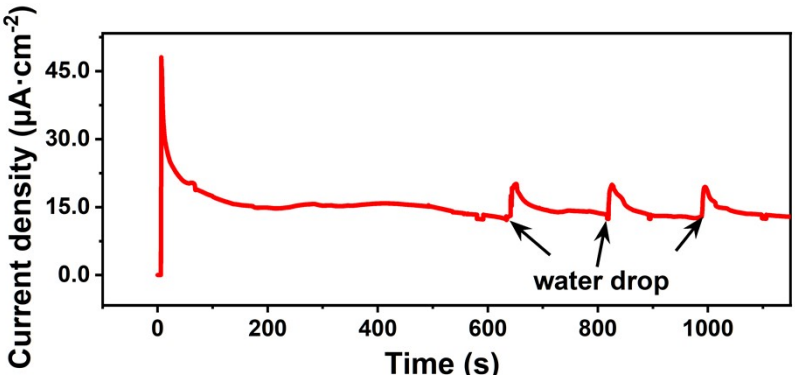

Fig. S8. Short-circuit current curve of 3D hierarchical TiO_2 nanoflowers-based WDHPGs under subsequent water droplet.

Supporting Information 13. Response to factors that influence the speed of water evaporation/infiltration

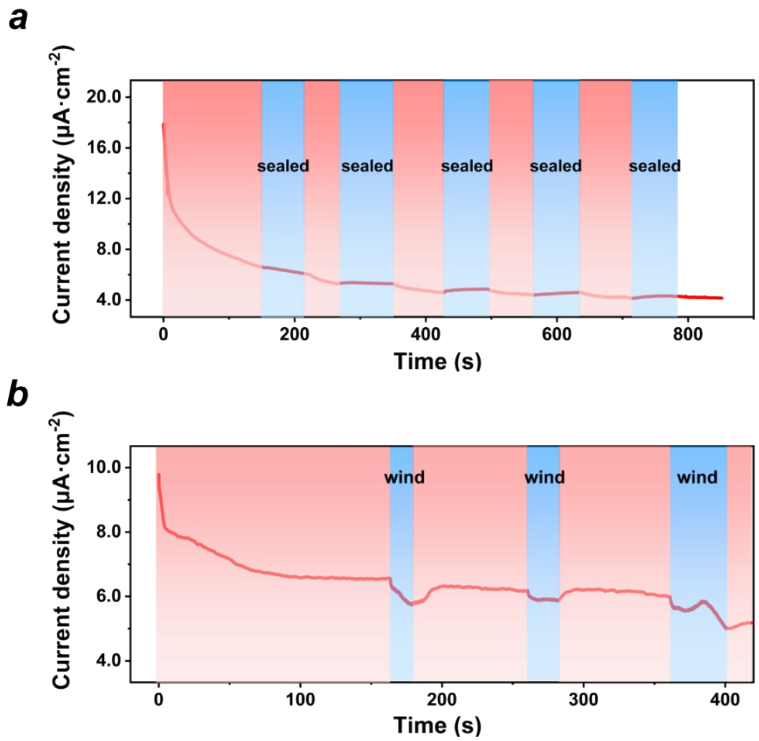

Fig. S9. Short-circuit current change of 3D hierarchical TiO_2 nanoflowers-based WDHPGs (a) in closed (blue bottom) /open (pink bottom) systems and (b) with (blue bottom) /without wind flow (pink bottom).

Supporting Information 14. ANOVA results of different influential factors

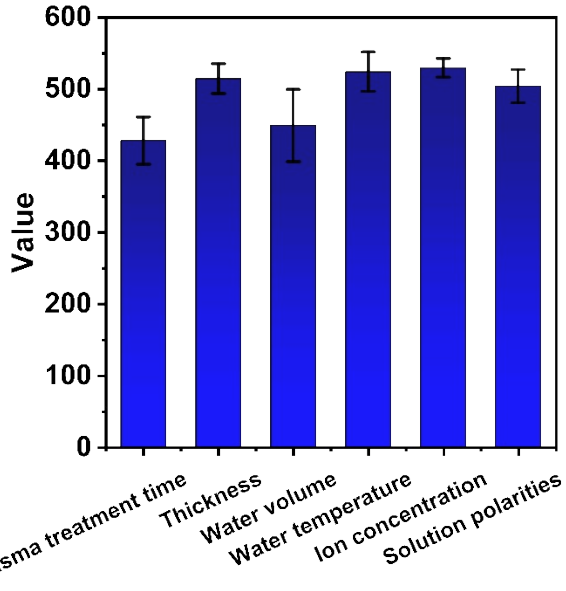

Fig. S10. Analysis of variance (ANOVA) results for different factors (mean ± standard error of the mean).

Supporting Information 15. Electrochemical testing of the WDHPGs

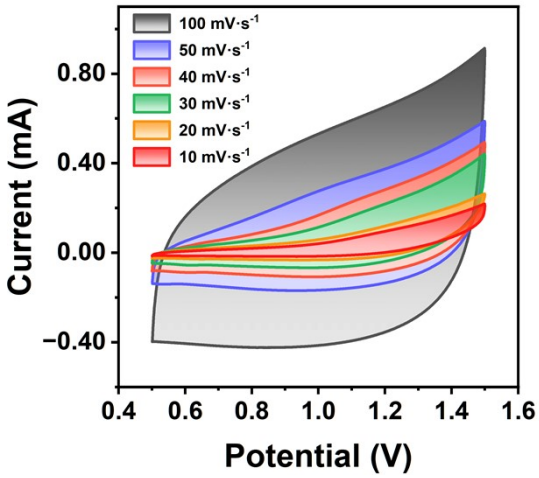

Fig. S11. Cyclic voltammetry (CV) scanning curves of 3D hierarchical TiO_2 nanoflowers-based WDHPGs with different scan rates.

Supporting Information 16. Physical and chemical stability of the 3D hierarchical TiO_2 flowers after times of cycling test

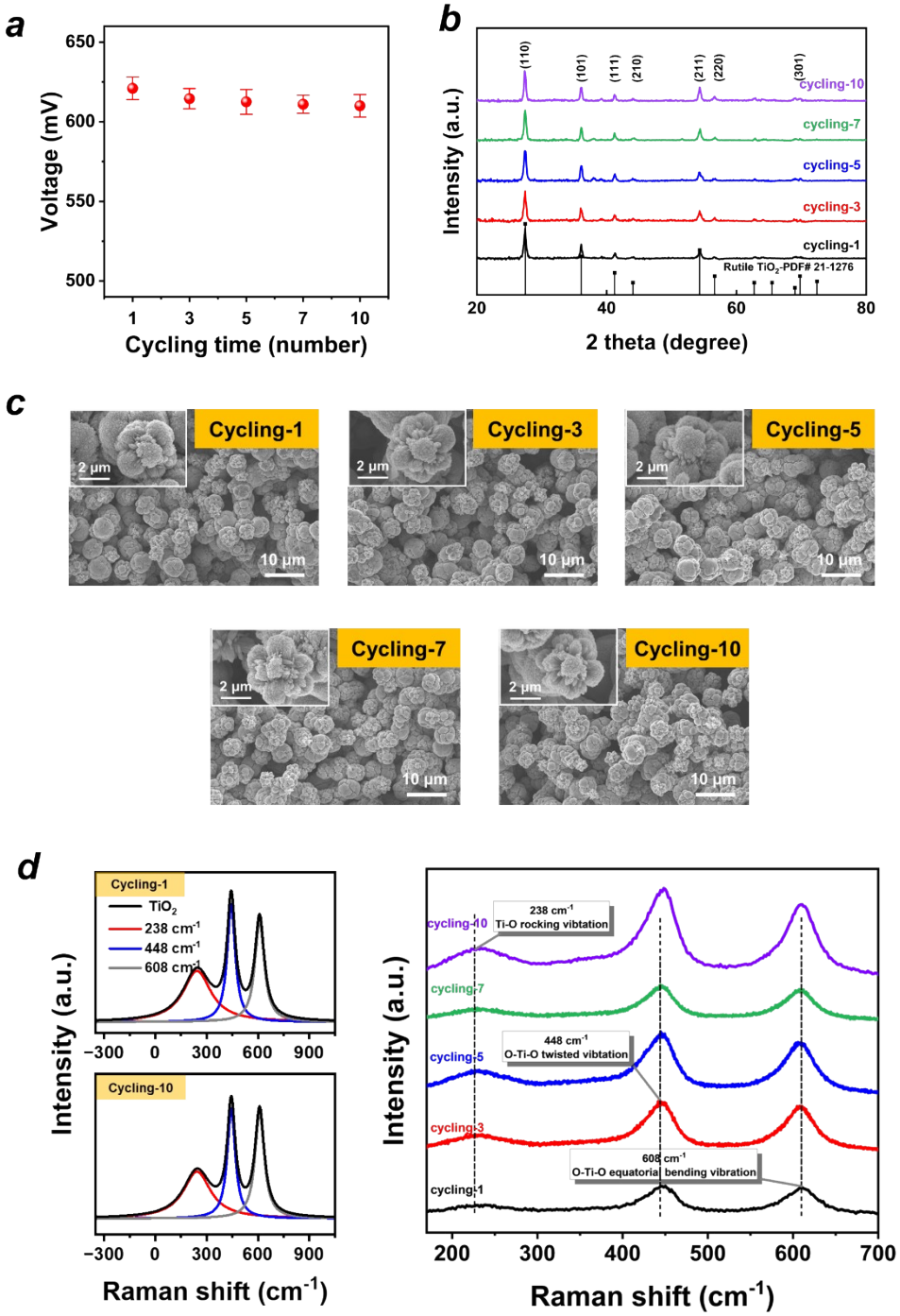

Fig. S12. (a) Output voltage, (b) XRD patterns, (c) SEM images, and (d) Raman spectra of HTNFs-based WDHPGs with different cycling times.

Supporting Information 17. Morphology of 3D HTNFs with different precursor concentrations

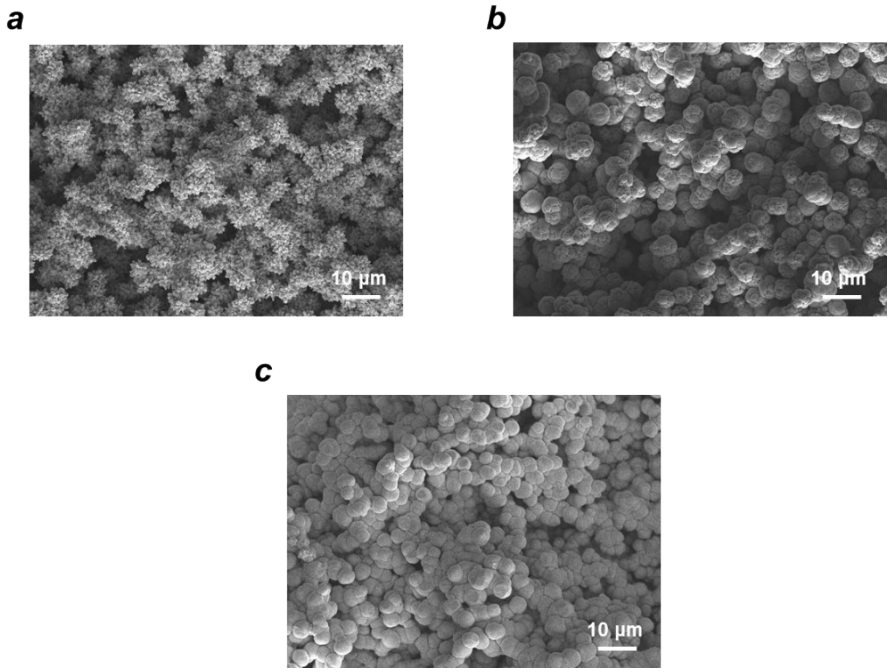

Fig. S13. Low-magnification SEM images of 3D hierarchical TiO_2 nanoflowers with a TBOT-HCl ratio of (a) 0.03:4 (HTNFs-3), (b) 0.06:4 (HTNFs-6), and (c) 0.09:4 (HTNFs-9).

Supporting Information 18. Detailed interface information of 3D HTNFs with different precursor concentrations

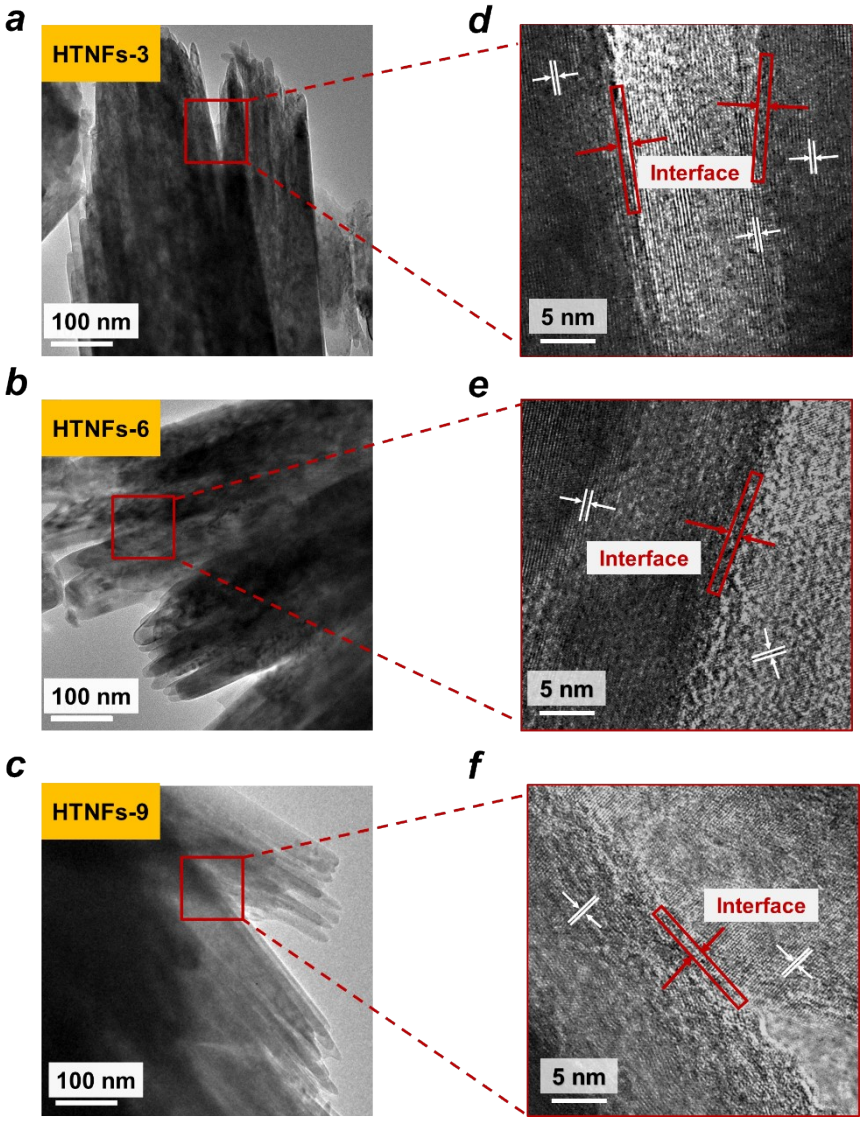

Fig. S14. TEM and high-resolution TEM (HRTEM) images of hierarchical TiO_2 nanoflowers with TBOT-HCl: ratio of (a, d) 0.03:4 (HTNFs-3), (b, e) 0.06:10 (HTNFs-6), and (c, f) 0.09:10 (HTNFs-9).

Supporting Information 19. Pore structure characterization of 3D HTNFs with different precursor concentrations

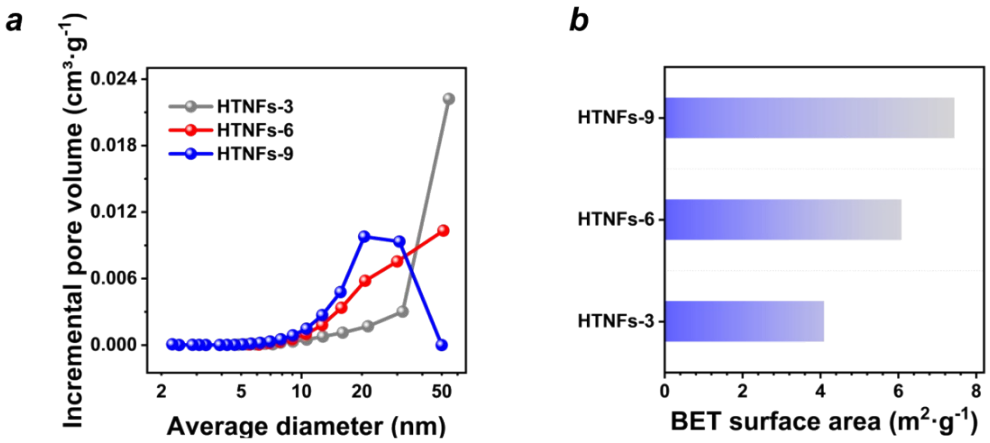

Fig. S15. Supplementary pore structure characterization. (a) Incremental pore volume versus pore diameter curve and (b) BET-specific surface area of HTNFs with different TBOT-HCl solution ratios (0.03:4, 0.06:4, 0.09:4).

Supporting Information 20. Water evaporation rate of HTNFs with different precursor concentrations

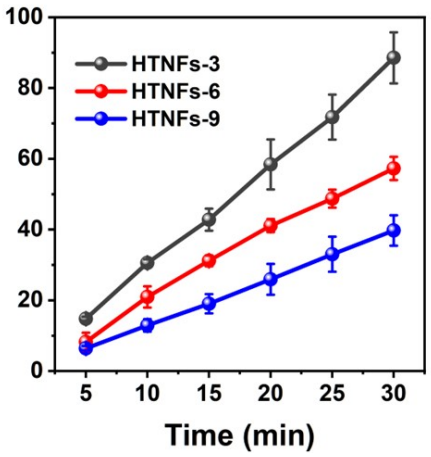

$$Evaporation\ ratio = \frac{weight\ of\ evaporated\ water}{initial\ weight\ of\ water}$$.

Fig. S16. Water evaporation rate of 3D HTNFs with different TBOT-HCl solution ratios (0.03:4, 0.06:4, 0.09:4).

Supporting Information 21. Electrochemical impedance spectra (EIS) of WDHPGs with different precursor concentrations

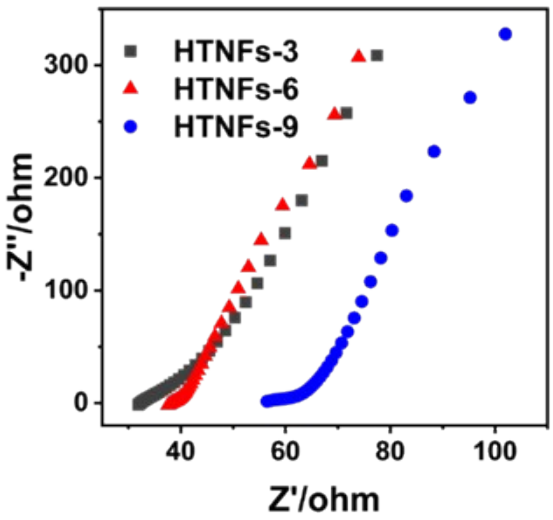

Fig. S17. Magnified electrochemical impedance spectra (EIS) of WDHPGs with different TBOT-HCl solution ratios.

Supporting Information 22. WDHPGs working as a power source

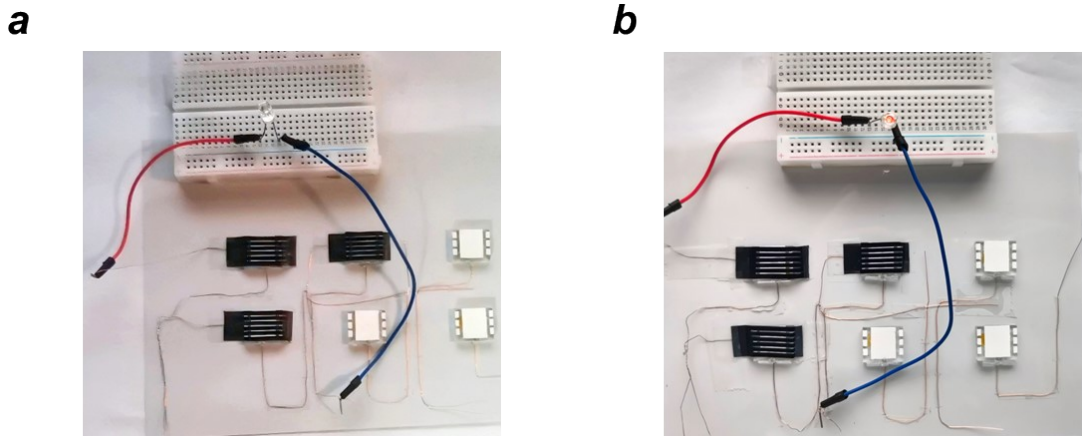

Fig. S18. Optical images of the red light-emitting diode (LED) (1.8 V) driven by three hierarchical TiO_2-based WDHPGs in series (a) before and (b) after water-dripping.

Supporting Information 23. WDHPGs working as a power source

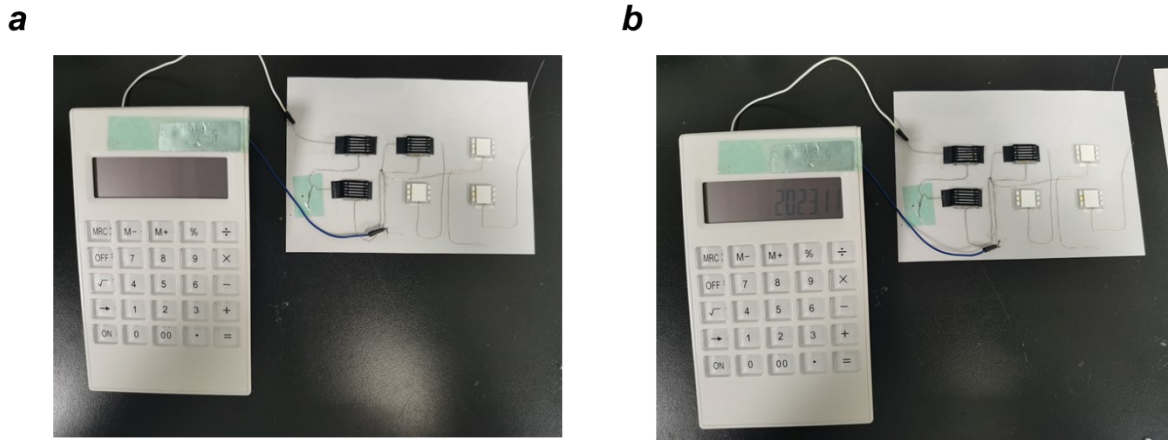

Fig. S19. Complete optical images of a commercial digital calculator driven by three hierarchical TiO_2 nanoflowers-based WDHPGs in series. (a) before and (b) after water-dripping.

Supporting Information 24. Electricity output performance of the 3D HTNFs-based WDHPGs with UV light illumination

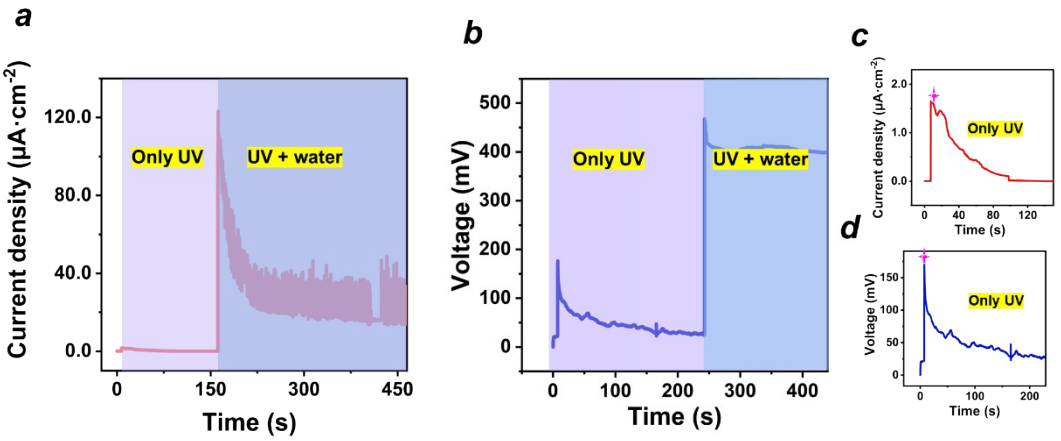

Fig. S20. (a) I_{sc} and (b) V_{oc} curve of hierarchical TiO_2 nanoflowers-based WDHPGs with UV first and subsequent water dripping. The amplification of peak (c) I_{sc} and (d) V_{oc} with UV light excitation only.

Supporting Information 25. Schematic illustration of the non-contact human-machine interface

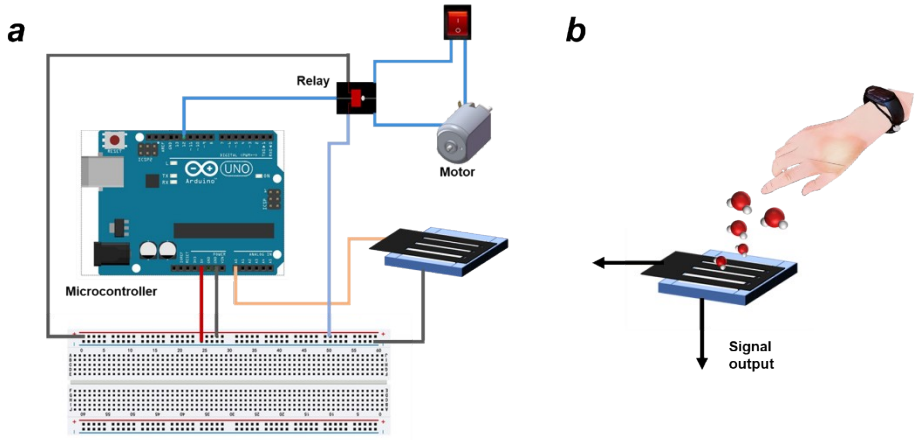

Fig. S21. Schematic illustration of (a) the non-contact interaction system that can drive a motor through the humidity signal and (b) the reception and output process of finger humidity.

Supporting Information 26. Schematic illustration of the self-powered humidity sensing system

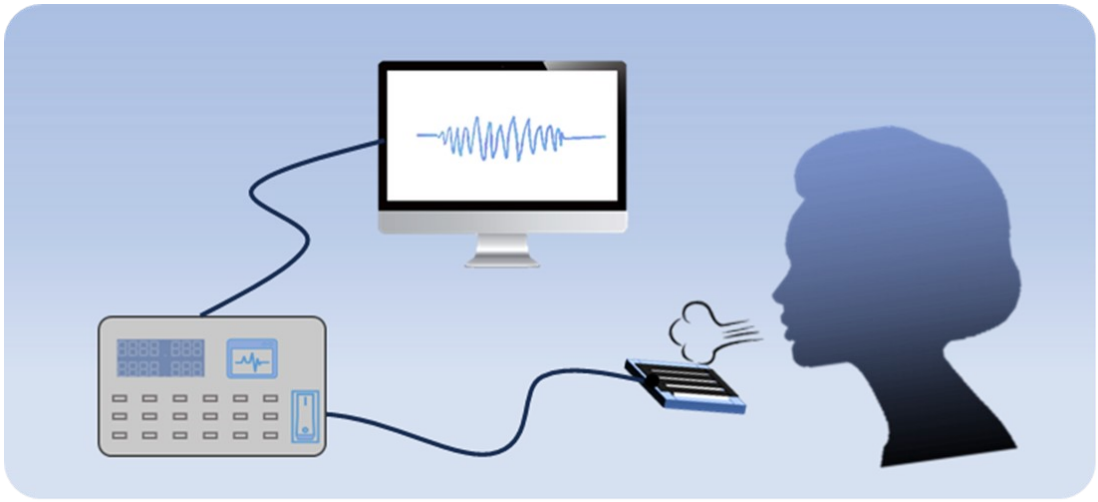

Fig. S22. Schematic illustration of the electrical signal measurement system of 3D HTNFs-based self-powered humidity sensors.

Supporting Information 27. Demonstration movies

Movie S1 Demonstration of the color change of 3D HTNFs surface by dripping phenol red

Movie S2 Demonstration of the output change of the 3D HTNFs–based WDHPGs with extra UV irradiation

Movie S3 Demonstration of the non-contact human-machine interface constructed of the 3D HTNFs-based device

Reference

[1] L. Ding, D. Xiao, Z. Lu, J. Deng, Y. Wei, J. Caro, H. Wang, *Angew. Chem. Int. Ed.* **2020**, *59*, 8720.

[2] H. S. White, A. Bund, *Langmuir* **2008**, *24*, 2212.

[3] T. Zhong, H. Li, T. Zhao, H. Guan, L. Xing, X. Xue, *Journal of Materials Science & Technology* **2021**, *76*, 33.

[4] Y. Hou, X. Zhang, C. Liu, C. Yin, Z. Yin, *Nano Energy* **2023**, *110*, 108338.

[5] D. Shen, M. Xiao, G. Zou, L. Liu, W. W. Duley, Y. N. Zhou, *Adv. Mater.* **2018**, *30*, 1705925.

[6] C. Shao, B. Ji, T. Xu, J. Gao, X. Gao, Y. Xiao, Y. Zhao, N. Chen, L. Jiang, L. Qu, *ACS Appl. Mater. Interfaces* **2019**, *11*, 30927.

[7] X. Zhao, Z. Xiong, Z. Qiao, X. Bo, D. Pang, J. Sun, J. Bian, *Chemical Engineering Journal* **2022**, *434*, 134671.

[8] B. Ji, N. Chen, C. Shao, Q. Liu, J. Gao, T. Xu, H. Cheng, L. Qu, *J. Mater. Chem. A* **2019**, *7*, 6766.

[9] Y. Qin, Y. Wang, X. Sun, Y. Li, H. Xu, Y. Tan, Y. Li, T. Song, B. Sun, *Angew. Chem.* **2020**, *132*, 10706.

[10] B. Shao, Z. Song, X. Chen, Y. Wu, Y. Li, C. Song, F. Yang, T. Song, Y. Wang, S.-T. Lee, B. Sun, *ACS Nano* **2021**, *15*, 7472.